Microwave–Assisted Synthesis of Nanoscale Tungsten Trioxide Hydrate with Excellent Photocatalytic Activity under Visible Irradiation

Xu–Teng Yu[a,‡], Heng–Xin Liu[a,‡], Yanhua Shen[b,‡], Jian–Ying Xu[a], Feng–Ying Cai[a], Taohai Li[b,c*], Jian Lü[a,d**] and Wei Cao[c]

[a]*Fujian Provincial Key Laboratory of Soil Environmental Health and Regulation, College of Resources and Environment, Fujian Agriculture and Forestry University, Fuzhou 350002, P.R. China*

[b]*College of Chemistry, Key Lab of Environment Friendly Chemistry and Application in Ministry of Education, Xiangtan University, Xiangtan, 411105, P.R. China*

[c]*Nano and Molecular Systems Research Unit, Faculty of Science, P. O. Box 3000, University of Oulu, FIN–90014, Finland*

[d]*Samara Center for Theoretical Materials Science (SCTMS), Samara State Technical University, Samara 443100, Russia*

[‡]*These authors contribute equally.*

[*]Corresponding author. E–mail addresses: hnlth@xtu.edu.cn (T.L.)

[**] Corresponding author. E–mail addresses: jian_lu_fafu@163.com (J.L.).

ABSTERCT:

Tungsten trioxide hydrate **(**WO_3•1/3H_2O) nanoparticles (NPs) were prepared via a microwave–assisted synthetic pathway by using Na_2WO_4•2H_2O and $PdCl_2$ as precursors. Microstructure and morphology of as–prepared WO_3•1/3H_2O NPs were investigated through X–ray diffraction patterns (XRD), transmission electron microscopy (TEM), and Fourier transform infrared (FT–IR) spectra, while porosity and bandgap through specific surface area and UV–vis absorption spectroscopy. It was found that Pd^{2+} ions played a crucial role in the formation of WO_3•1/3H_2O NPs, and thus a possible formation mechanism was proposed based on the growth processes. The photocatalytic property of WO_3•1/3H_2O NPs were evaluated on the basis of Rhodamine B (RhB) degradation in aqueous solutions under simulated visible irradiation. The photocatalytic experimental results indicated that as–prepared WO_3•1/3H_2O NPs exhibited much more superior photocatalytic activity by contrast to that of the commercial WO_3.

Keywords: Tungsten trioxide; Nanoparticle; Photocatalysis; Microwave–assisted synthesis; Dye degradation

Low–dimensional nanomaterials, e.g. nanoparticles, nanorods, and nanotubes, have been within the research focus of functional materials due to their unique physical and chemical properties in comparison with their bulk counterparts. A wide range of advanced applications has been developed based on these novel nano–complexes [1–3]. Many low–dimensional nanostructures can be synthesized through self–assembled growth by means of simple and spontaneous processes, paving a facile route for their applications in large scales. Among the various low–dimensional materials, semiconductor metal oxides have attracted tremendous attentions because of their distinctive utilities in optics and electronics. For instance, the tungsten trioxide (WO_3) in nanoparticle form is an n–type indirect wide band gap material [4, 5]. Due to high work function, WO_3 has been employed as a charge injection layer [6], further to the high catalytic activity that enables WO_3 to be used for photocatalytic and electrocatalytic purposes [7, 8]. Furthermore, thanks to hosting abilities for ions, WO_3 is widely used in electrochemical Li ion batteries, electrochromic, thermochromic, and photochromic devices [9–12].

A number of chemical and physical methods have been developed for the synthesis of low–dimensional WO_3 nanostructures including hydrothermal/solvothermal synthesis [13–16, 9, 17], hot–wire chemical vapor deposition [18], spray pyrolysis [19], template mediated synthesis [14], sol–gel method [20–22] and micro–emulsion technique [23]. Among these techniques, the microwave heating route distinguishes itself from other conventional methods with the following features: (i) microwave heating enables a new heating way down to molecular levels, even at small temperature gradient through molecular dynamics; (ii) the adjustable heating characteristics of microwave can precisely tune vapor–phase temperatures, improving selectivity of reactions; (iii) the microwave heating has little residual heat. When power generator is switched off, the microwave

immediately stops. The non–delayed effect makes the reactions with higher demand for controlling temperature progress; and (iv) the high–speed heating accelerates the speed of disposing materials, offering a very good efficiency of energy utilization. Thus, microwave–assisted synthesis may result in a high–speed, low–cost, pollution–free and high–efficient method for the preparation of inorganic oxide semiconductor–tungsten trioxide. Several studies have been reported in literatures towards the preparation of WO_3 powders via microwave–assisted methods. Hernandez–Urestia et al. described a hydrothermal method without the use of any additives during the synthesis of WO_3 nanoparticles [24]. The products exhibit either hexagonal or monoclinic structures by varying the time (30 or 60 min) of microwave hydrothermal reactions. Recently, doping of metal ions in WO_3 represents a promising means to enhance their excellent catalytic activities. Hence, various metal ions such as Co^{2+}, Cu^{2+}, Zn^{2+}, Cr^{3+} and Ti^{4+} have been tentatively doped into WO_3 nanomaterials [25–29]. For example, Kovendhan reported that 5% Li–doped WO_3 resulted in blue–shift of photoemission and structural change from the orthorhombic to tetragonal phase [30]. Boubaker investigated the Zn/In–doped WO_3 and proposed that quantum–linked lattice disorder could influence the final photoresponse [31]. Despite of above achievements, very few investigations have been carried out to study the effect of cation or anion of salts on the formation of WO_3.

In the present work, tungsten trioxide hydrate WO_3•$1/3H_2O$ nanoparticles were synthesized through a facile microwave–assisted hydrothermal method by which the morphology of nanomaterials was controlled. Based on the experimental results, we discovered that Pd^{2+} ions played a crucial role in the formation of the WO_3•$1/3H_2O$ nanostructures, and thus a possible formation mechanism were proposed. In addition, the photocatalytic activity of as–prepared WO_3•$1/3H_2O$ was investigated, which was much superior to that of the commercial WO_3, for Rhodamine B (RhB)

degradation in aqueous solutions under simulated visible irradiation. These results indicated that the as–prepared WO_3•1/3H_2O nanostructures possessed great potentials as visible–light–driven photocatalysts.

Sodium tungstate dihydrate (Na_2WO_4•2H_2O), palladium chloride ($PdCl_2$), palladium acetate palladium acetate ($Pd(AC)_2$), cobalt chloride anhydrous ($CoCl_2$), Rhodamine B (RhB), methyl orange (MO), methylene blue (MB) and absolute ethanol were commercially purchased and used without further purification or modification. Reaction and stock solutions were prepared by using deionized water provided with a UPT–I–5T ultrapure water system.

The X–ray powder diffraction (XRD) was performed by using a MiniFlex II X–ray diffractometer operated at 40 kV and 40 mA to get the Cu Kα_1 (λ= 0.15406 nm) line as the incident source. The XRD data were recorded at the 2θ range of 5–70° with a scan rate of 0.02° s^{-1}. Transmission electron microscopy (TEM) images were obtained on a JEOL JEM–2100 microscope with a LaB6 filament at an accelerating voltage of 200 kV. The specific surface area was calculated using the Brunauer–Emmett–Teller (BET) method based on the nitrogen adsorption isotherm obtained at 77 K in a constant volume adsorption apparatus (2020 M). FTIR spectra were recorded in the range of 400–4000 cm^{-1} at a step of 2.0 cm^{-1} and KBr as pellets. The UV–vis absorption spectra were recorded on a Lambda 25 UV–vis spectrophotometer (Perkin–Elmer, USA) in the range of 200–800 nm. Diffuse reflectance spectra (DRS) were recorded on a Shimadzu UV–vis spectrophotometer (UV–2550) with $BaSO_4$ as the background. X–ray photoelectron spectroscopy (XPS) measurements were performed on a Thermo Fisher ESCALAB 250Xi spectrometer with Al Kα X–ray source (15 kV, 10 mA).

To synthesize WO_3·1/3H_2O nanomaterials, 330 mg sodium tungstate dihydrate (Na_2WO_4•2H_2O)

and 178 mg palladium chloride ($PdCl_2$) were dissolved in 10 mL deionized water. Vigorous stirring and ultrasonic disperse were necessary to ensure that starting materials were dispersed homogeneously in the deionized water, and then the mixture was heated under microwave irradiation at different reaction temperatures (140 ºC, 160 ºC and 180 ºC). After cooling down to room temperature naturally, the precipitate was collected by centrifugation, and washed several times with deionized water and absolute ethanol. Finally, the precipitation was dried in a vacuum oven at 50 ºC for 12 h.

The photochemical reactor consists of an optical quartz glass beaker surrounded by a water jacket to keep the reaction at room temperature. The photocatalytic activity of as–prepared WO_3•$1/3H_2O$ catalysts were evaluated for the degradation of RhB (10 mg L^{-1}) under visible light irradiation (Xe–lamp, 300 W) with the 400 nm cutoff filter. Typically, 50 mg of the catalyst and 100 mL of aqueous dye solution were mixed with stirring. The adsorption–desorption equilibrium of dye molecules on catalyst surfaces was reached by keeping the solution in dark for 30 min. During a catalytic process, 3.0 mL of the suspension was extracted at certain time of reaction to record with UV–vis spectra. The RhB concentrations were evaluated initially and at certain time intervals for kinetics study. The RhB degradation efficiency was calculated using the following equation:

$$\eta = (1 - C_i / C_0) \times 100 \qquad (\mathbf{1})$$

where C_0 is the initial concentration and C_i the concentration after a certain time of reaction.

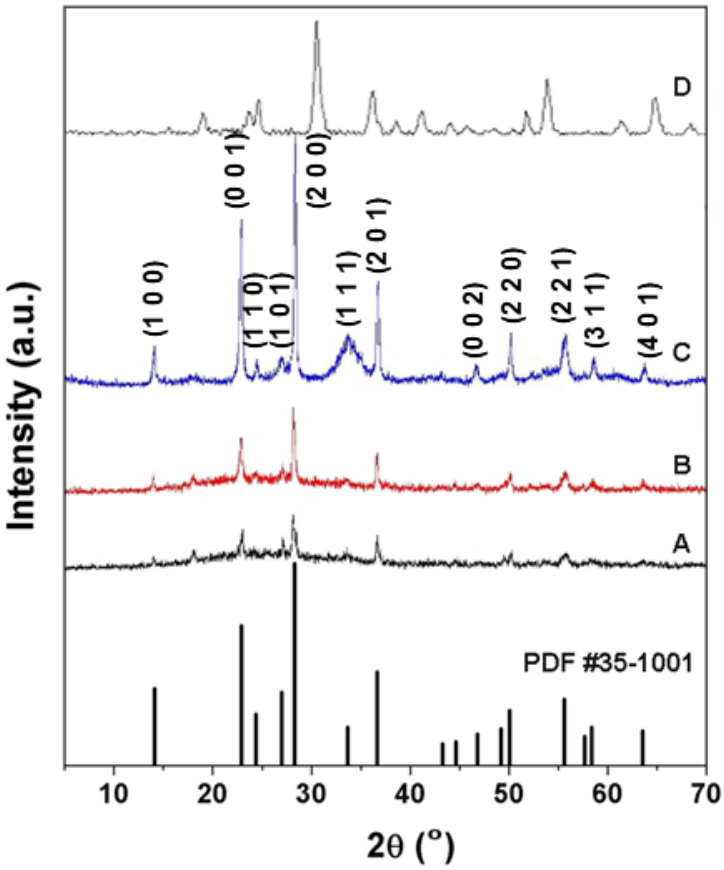

Fig. 1. XRD patterns of as–prepared W–140 **(A)**, W–160 **(B)**, W–180 **(C)** and R3 product **(D)**.

In order to verify the crystalline phases of tungsten trioxides prepared by the microwave–assisted hydrothermal method at different reaction temperatures with the same reaction time of 20 min. The overall crystallinity and purity of the nanomaterials were examined by X–ray diffraction (XRD), as in Fig. 1. All diffraction peaks were indexed to the pure phase of the WO_3•1/3H_2O according to the JCPDS Card no. 35–1001. Fig. 1A, 1B and 1C correspond to the XRD patterns of WO_3•1/3H_2O nanomaterials prepared at 140 ºC (W–140), 160 ºC (W–160) and 180 ºC (W–180), respectively. The relative peak intensity of the three materials varied significantly. It was found that the crystallization of WO_3•1/3H_2O samples could be controlled by varying reaction temperatures with a set reaction time (20 min). In general, the WO_3•1/3H_2O showed better crystallinity with the increase of reaction temperature. The results illustrated that the increase of

temperature by microwave radiation was beneficial for the crystallization of tungsten trioxide nanomaterials and the well–crystallized WO_3•1/3H_2O was prepared at 180 ºC for 20 min (W–180). The X−ray photoelectron spectroscopy (XPS) technique was applied to reveal surface compositions and valence state of elements in WO_3•1/3H_2O samples (Fig. 2). Taking the XPS spectra of W–160 as a representative, the strong peak at 530.5 eV was attributed to the lattice O atoms of WO_3, and the shoulder peaks at 531.8eV and 534.1 eV corresponded to the oxygen atoms in chemically adsorbed H_2O and OH groups (Fig. 2A). The doublet peaks at 35.4 eV (W $4f_{7/2}$) and 37.5 (W $4f_{5/2}$) were characteristics of W(VI) species [14] (Fig. 2B).

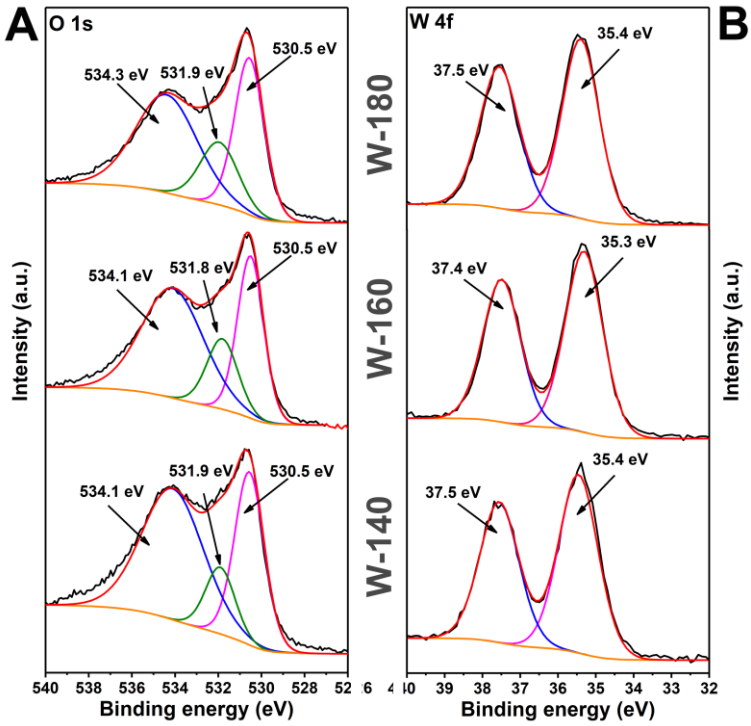

Fig. 2. XPS spectra of WO_3•1/3H_2O nanomaterials: **(A)** O1s **(B)** W4f.

It has been recognized that the size and shape of nanoscale photocatalyst particles profoundly affect their reaction performance. Therefore, the microstructure of WO_3•1/3H_2O nanomaterials were confirmed through the scanning electron microscope (SEM) and transmission electron microscope

(TEM) determinations. Fig. 3A shows the typical SEM morphologic image of WO_3•1/3H_2O nanomaterials (W–160). TEM and high–resolution TEM (HR–TEM) images clearly revealed that the WO_3•1/3H_2O possessed nanoscale structures with particle sizes below 5.0 nm (Fig. 3B and 3C), which also suggested the formation of crystalline hexagonal phase of tungsten trioxide hydrate with crystal plane spacing of 0.203 nm corresponding to the (2 1 1) lattice plane (Fig. 3C). The SAED pattern of the sample was highly symmetric (Fig. 3D), indicating single crystal characteristics of single nanoparticles.

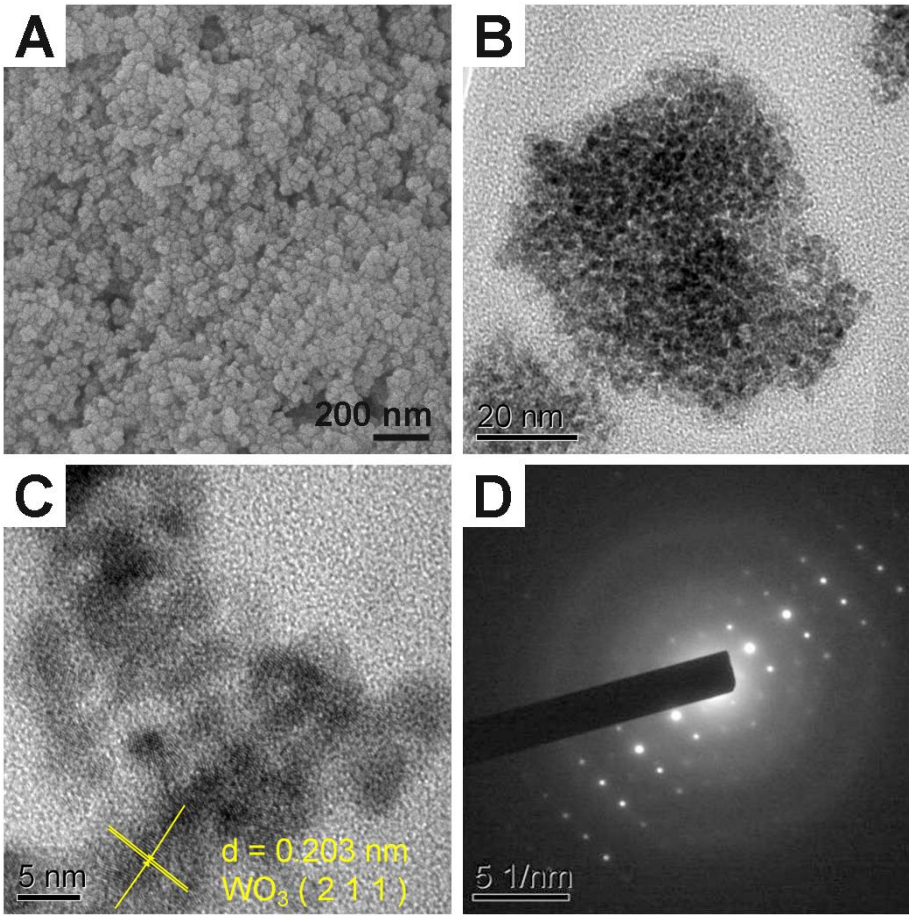

Fig. 3. Typical SEM **(A)**, TEM **(B)**, high–resolution TEM **(C)** and SAED **(D)** images of as–prepared WO_3•1/3H_2O.

The bonding structure of the WO_3•1/3H_2O samples was studied through the FT–IR spectra. As

shown in Fig. 4A a representative, the structure of W–160 consisted of packed corner–sharing WO_6 octahedra that had three vibration modes in the IR region of 900–600, 400–200 and < 200 cm^{-1}, which corresponded to the O–W–O stretching, bending and lattice modes [32]. Two peaks at 661 and 888 cm^{-1} were assigned as a shortening of the W–O bonds of *hex*–WO_3. Additionally, a sharp peak was observed at 1617 cm^{-1}, while two narrow bands and a broad band at the range of 500–1000 cm^{-1}. The first groups of bands were caused by air contact (i.e. aging effect), as moisture could be readily absorbed at surfaces. The band in the range of 2800–3650 cm^{-1} and a peak at 1617 cm^{-1} belonged to υ(OH) and δ(OH) modes of adsorbed water molecules [33]. The Brunauer−Emmett−Teller (BET) surface areas of WO_3•1/3H_2O with different reaction temperature were examined by the N_2 adsorption/desorption (Fig. 4B), which showed typical type II isotherms. BET surface area of W–140, W–160 and W–180 was calculated to be 73.7 m^2 g^{-1}, 169 m^2 g^{-1} and 176 m^2 g^{-1}, and Langmuir surface area to be 114 m^2 g^{-1}, 262 m^2 g^{-1} and 271 m^2 g^{-1}, respectively, which was comparable to WO_3•1/3H_2O samples reported in the literature [14,31]. The N_2 adsorption/desorption isotherms also indicated typical adsorption behaviors of nanomaterials. As a result, the WO_3•1/3H_2O samples showed considerable surface areas, which could affect their photocatalytic properties.

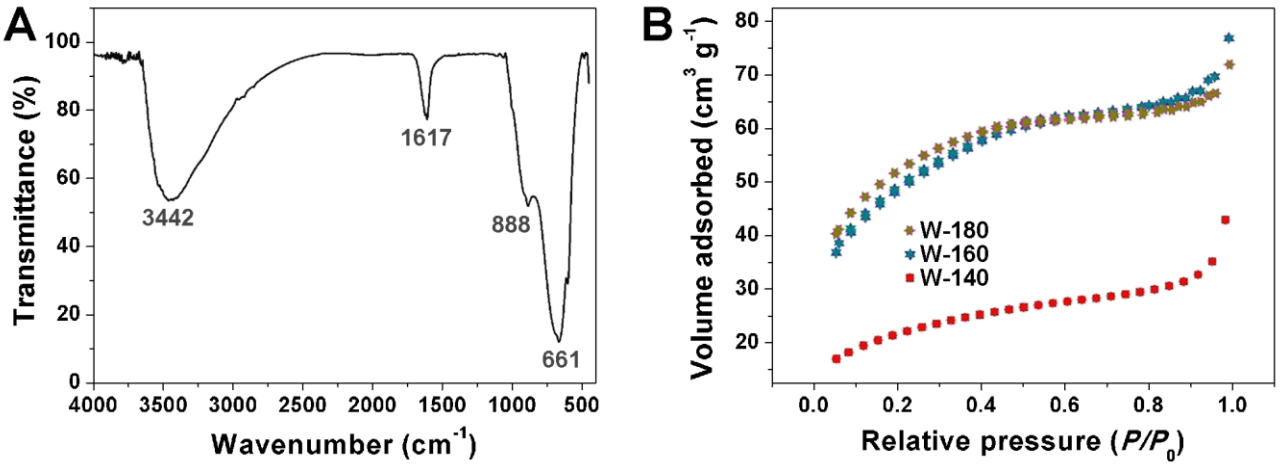

Fig. 4. (A) The FT–IR spectrum of the W–160; and **(B)** nitrogen adsorption/desorption isotherms of as–prepared WO_3•1/3H_2O samples.

In general, reaction temperature is a very important parameter determining the phase of low–dimensional nanomaterials produced from the microwave–assisted hydrothermal process. The anisotropic growth of nanoparticles can be explained by the specific adsorption of ions to particular crystal surfaces, inhibiting the growth of these faces by increasing their surface energy. Herein, it was likely that the presence of Pd^{2+} was responsible for the formation of WO_3•1/3H_2O nanostructures with high aspect ratios [34]. These ions act as capping agents to control the growth rate of different crystal faces through a selective adsorption process. Based on the above experimental results, the $PdCl_2$ was believed to play a crucial role in the formation of the WO_3•1/3H_2O nanostructures. Formation of WO_3•1/3H_2O nanostructures could be represented as follows [35, 36]:

$$Na_2WO_4 + PdCl_2 + (n+2)H_2O \rightarrow H_2WO_4{\bullet}nH_2O + 2NaCl + Pd(OH)_2$$

$$H_2WO_4{\cdot}nH_2O \rightarrow WO_3 + (n+1)H_2O$$

To study the effect of cation and anion of salts on the formation of WO_3•1/3H_2O nanostructures, additional syntheses were carried out with $Pd(AC)_2$ or $CoCl_2$ as the substitution of $PdCl_2$. The selected materials and the factors of reactions are summarized in Tab. 1.

Tab. 1. Reaction reactants and parameters for the formation of WO_3•1/3H_2O.

Sample	**Reactant (mg)**			**Temperature**	**Time**	**Solvent**	**pH**
	Na_2WO_4•2H_2O	$Pd(AC)_2$	$CoCl_2$			H_2O	
R1*	330	0	0	160 ºC	20 min	10 mL	8.2–8.2
R2	330	224	0	160 ºC	20 min	10 mL	6.7–5.4

R3	330	0	130	160 ºC	20 min	10 mL	7.0–6.2

*R represents the experimental entry.

Supernatant liquid, brown mixture and blue blade precipitation were obtained as products from entries R1, R2 and R3, respectively, at the end of reactions. The samples were centrifuged and washed with distilled water and absolute ethanol to remove ions possibly remaining in products, followed by drying at 50 ºC in air for 12 h. The brown mixture sample R2 was demonstrated to be an amorphous phase. The XRD analysis of product from sample R3, as shown in Fig. 1D, could not match the pattern of WO_3•1/3H_2O. On the basis of above analysis, we concluded that Pd^{2+} was crucial for the formation of WO_3•1/3H_2O nanomaterials.

The photocatalytic activity of WO_3•1/3H_2O samples were evaluated for RhB degradation as a model reaction under visible light irradiation [37, 38], by monitoring the maximum absorbance of RhB at 552 nm (Fig. 5A). The photodegradation of RhB is shown in Fig. 5B for W–140, W–160 and W–180, respectively. Noticeable changes of maximum absorption characteristics were observed upon visible irradiation for 6 h. The photodegradation efficiencies of RhB for W–140, W–160 and W–180 were ca. 82.2%, 92.8% and 89.1%, respectively, whereas commercial WO_3 achieved only 66.1% of RhB degradation under the same conditions (Fig. 5B). By contrast, the W–160 displayed much superior (ca. 1.4 times) photocatalytic efficiency for RhB degradation. To estimate the rate of reactions, kinetic experiments were performed to study the photocatalytic degradation of the RhB. The kinetics equation can be expressed as follows:

$$\eta = \ln (A_0 / A_t) = \ln (C_0 / C_i) = kt \qquad (2)$$

where A_0 and A_t are corresponding maximum absorption of RhB measured at the initial concentration

and at different illumination time, *k* the reaction rate constant, and *t* the reaction time. The reaction rate (*k*) was calculated from all photodegradation experiments by ln (C_0 / C_i) versus *t*, as shown in Fig. 5C. Rate constant (*k*) were estimated to be 0.721 (commercial WO_3), 0.816 (W–140), 1.81 (W–160) and 1.43 (W–180) min^{-1}. Bsed on these results, the W–160 sample exhibited the best photocatalytic performance, which was in accordance with BET analyses.

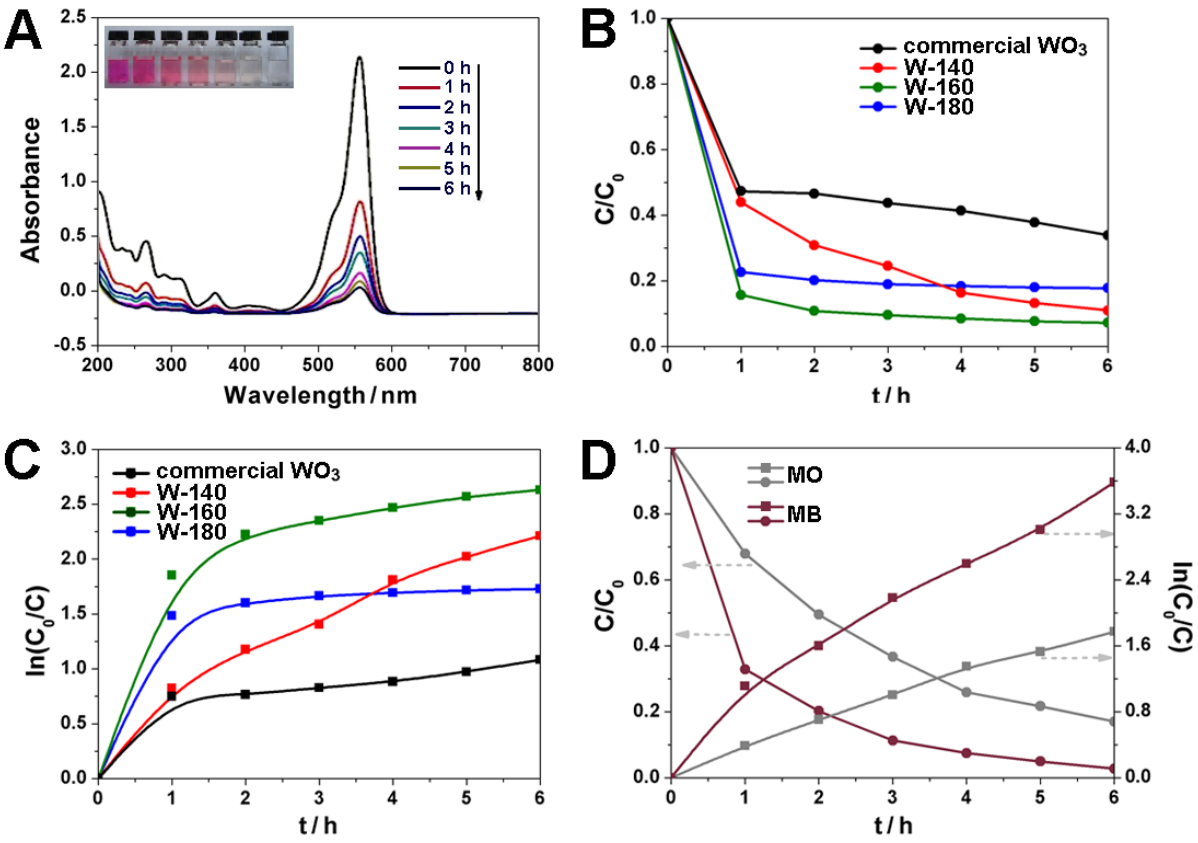

Fig. 5. (A) Typical UV–Vis absorption spectrum of the RhB solution under visible irradiation; **(B)** decolorization rates of RhB solutions with different materials; **(C)** plot of ln (C_0/C) as a function of irradiation time in the presence of various photocatalysts; and **(D)** photocatalytic degradation of MO and MB with W–160.

In order to further demonstrate photocatalytic ability of the best–performing W–160 nanomaterial, photodegradation of methyl orange (MO, maximum absorbance at 464 nm) and methylene blue (MB, maximum absorbance at 664 nm) were further studied. As shown in Fig. 5D,

the W–160 showed considerable degradation efficiency towards MO (ca. 83.1%) and MB (ca. 97.2%) after illumination under visible irradiation for 6 h. Moreover, it should be noted that the as–prepared WO_3•1/3H_2O was found to be more active in the degradation of the organic pollutants under visible irradiation. Furthermore, UV−vis diffuse reflectance spectra (DRS) was measured to study the photoabsorption behavior of the W–160 (Fig. 6A), which exhibited absorption edges at ca. 662 nm and calculated by the Tauc equation, corresponding to the bandgap energy of ca. 2.32 eV. Mott–Schottky plots were employed to estimate the flat–band potentials (V_{fb}) of the W–160 photocatalyst. As shown in Fig. 6B, the intersection point was independent on frequency and flat band potential (V_{fb}) of W–160, which was estimated form the intersection to be–0.24 V vs. Ag/AgCl (–0.04 V vs. NHE). Therefore, the conduction band (CB) of W–160 was approximately –0.04V vs. NHE, and the valence band (VB) potentials of W–160 was ca. +2.32 V vs. NHE, calculated by the equation: E_{VB} = CB + E_g [39].

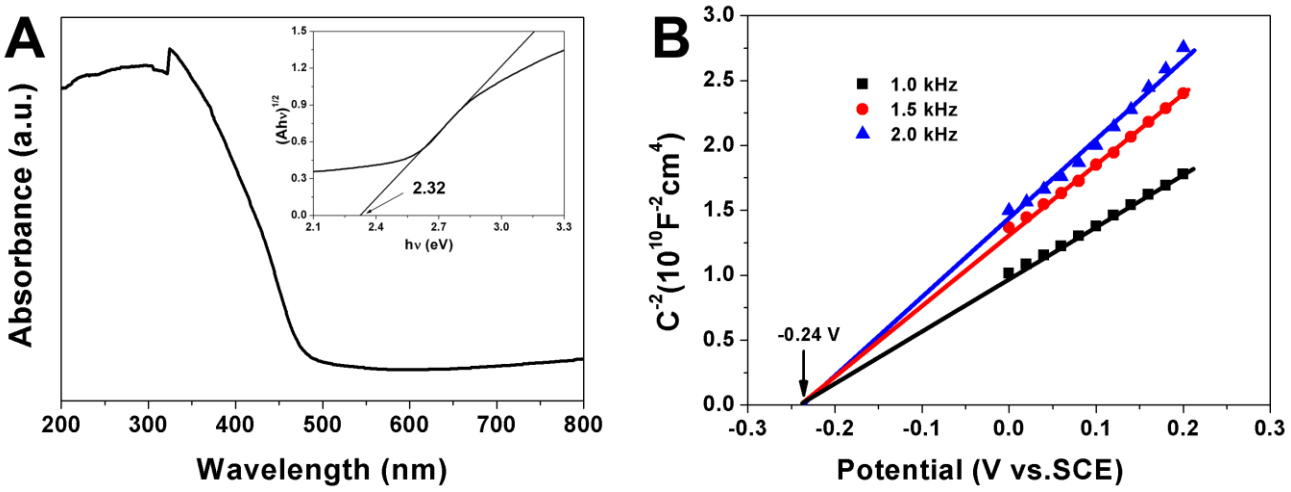

Fig. 6. (A) UV–Vis DRS and **(B)** Mott−Schottky plots for W–160.

For the photodegradation of organic dyes (RhB, MO and MB) shown by WO_3•1/3H_2O nanomaterials (the W–160 as a representative), a possible photocatalytic mechanism of

photocatalysis was proposed as shown in Scheme 1. The photocatalysts were activated by visible irradiation to generate pairs of electrons (e^-) and holes (h^+) [40–42]. Afterwards, the photogenerated holes reacted with H_2O to form hydroxyl radicals (•OH) and hydrogen ions (H^+), in which the hydroxyl radicals served as the main oxidant species to degrade the organic pollutants [43], while the generated hydrogen ions as a byproduct and resulted in the decrease of pH in the reactor. On the other hand, the photogenerated electrons consumed oxygen to create other oxidant species, which can be oxidized directly by active radicals to final products as H_2O and CO_2 [44]. For these reasons, the nanomaterial photocatalysts exhibited excellent photocatalytic efficiency. Overall, dye molecules are degraded by the active species as follows:

$$WO_3 + h\nu \rightarrow h^+ + e^-$$
$$h^+ + OH^- \rightarrow \bullet OH$$
$$h^+ + H_2O \rightarrow \bullet OH + H^+$$
$$e^- + O_2 \rightarrow \bullet O_2^-$$
$$\bullet O_2^- + H^+ \rightarrow H_2O\bullet \rightarrow O_2 + OH^- + \bullet OH$$
$$\text{Organic pollutants} + \bullet OH + O_2 \rightarrow CO_2 + H_2O$$

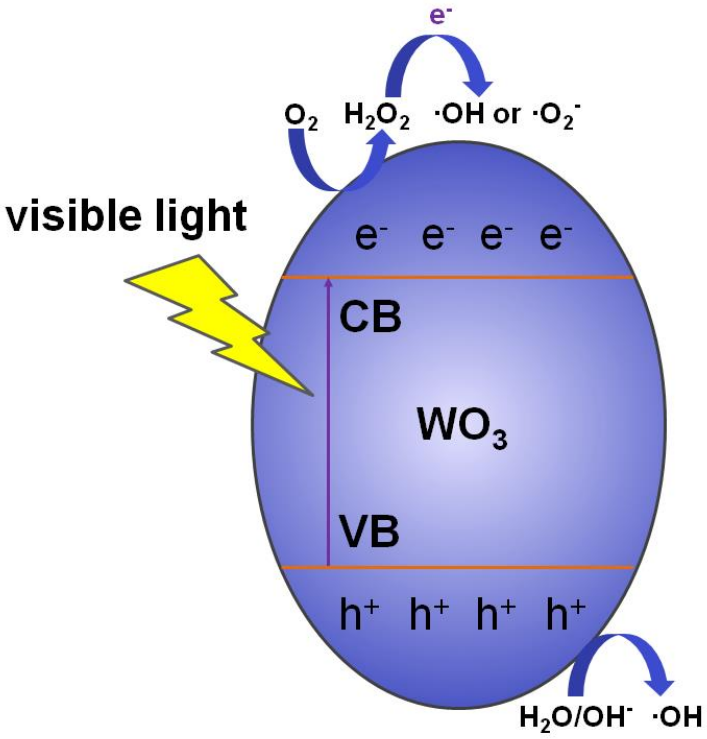

Scheme 1. Schematic illustration of the photocatalytic mechanism of WO_3•1/3H_2O under visible light irradiation.

In this work, nanostructured tungsten trioxide hydrates (WO_3•1/3H_2O) were successfully synthesized by a facile and fast microwave–assisted hydrothermal reaction and the structural, physicochemical and photocatalytic property of the nanomaterials were studied. It was concluded that Pd^{2+} cations played a crucial role in the formation of WO_3•1/3H_2O nanomaterials. Besides, the photocatalytic property of WO_3•1/3H_2O photocatalysts were closely related to the morphology, crystallization and surface modification. The as–prepared WO_3•1/3H_2O nanomaterials generally showed excellent photocatalytic ability than commercial WO_3 for the degradation of organic dyes. This work thus provides a viable pathway by using the microwave–assisted hydrothermal method to prepare functional nanomaterials for potential photocatalytic applications.

Acknowledgements

The authors acknowledge with thanks the financial support of the National Natural Science Foundation of China (grant no. 21601149), the International Science and Technology Cooperation and Exchange Project of Fujian Agriculture and Forestry University (grant no. KXGH17010), the Scientific Research Fund of Hunan Provincial Education Department (grant no. 16B253), the Open Project Program of State Key Laboratory of Structural Chemistry, China (grant no. 20150018 and 20170032), the Hunan 2011 Collaborative Innovation Center of Chemical Engineering & Technology with Environmental Benignity and Effective Resource Utilization, and the Oulu University Strategic Grant. T. L. acknowledges Oulu University Short–term International Research Visit grant during his stay in Finland.

References

[1] Z.F. Huang, J.J. Song, L. Pan, X.W. Zhang, L. Wang, J.J. Zou, Tungsten oxides for photocatalysis, electrochemistry, and phototherapy, Adv. Mater. 27 (2005) 5309–5327.

[2] D.D. Xu, T.F. Jiang, D.J. Wang, L.P. Chen, L.J. Zhang, Z.W. Fu, L.L. Wang, T.F. Xie, pH–dependent assembly of tungsten oxide three–dimensional architectures and their application in photocatalysis, ACS Appl. Mater. Interfaces. 6 (2014) 9321–9327.

[3] Y.S. Li, Z.L. Tang, J.Y. Zhang, Z.T. Zhang, Fabrication of vertical orthorhombic/hexagonal tungsten oxide phase junction with high photocatalytic performance, Appl. Catal. B: Environ. 207 (2017) 207–217.

[4] H. Aliasghari, A.M. Arabi, H. Haratizadeh, A novel approach for solution combustion synthesis of tungsten oxide nanoparticles for photocatalytic and electrochromic applications, Ceram. Int. 46 (2020) 403–414.

[5] M. Farjood, M.A. Zanjanchia, Template–free synthesis of mesoporous tungsten oxide nanostructures and its application in photocatalysis and adsorption reactions, ChemistrySelect. 4 (2019) 3042–3046.

[6] M. Hoping, C. Schildknecht, H. Gargouri, T. Riedl, M. Tilgner, H.H. Johannes, W. Kowalsky, Transition metal oxides as charge injecting layer for admittance spectroscopy, Appl. Phys. Lett. 92 (2008) 213306.

[7] J. Meng, Q.Y. Lin, T. Chen, X. Wei, J.X. Li, Z. Zhang, Oxygen vacancy regulation on tungsten oxides with specific exposed facets for enhanced visible–light–driven photocatalytic oxidation, Nanaoscale. 10 (2018) 2908–2915.

[8] X.N. Song, C.Y. Wang, W.K. Wang, X. Zhang, N.N. Hou, H.Q. Yu, A dissolution–regeneration route to synthesize blue tungsten oxide flowers and their applications in photocatalysis and gas sensing, Adv. Mater. Interfaces. 3 (2016) 1500417.

[9] K. Huang, Q. Pan, F. Yang, S. Ni, X. Wei, D. He, Controllable synthesis of hexagonal WO_3 nanostructures and their application in lithium batteries, J. Phys. D: Appl. Phys. 41 (2008) 155417.

[10] S.R. Bathe, P.S. Patil, Electrochromic characteristics of pulsed spray pyrolyzed polycrystalline WO_3 thin films, Smart Mater. Struct. 18 (2008) 025004.

[11] S.N. Alamri, Study of thermocolored WO_3 thin film under direct solar radiation, Smart Mater. Struct. 18 (2009) 025010.

[12] Z. Luo, J. Yang, H. Cai, H. Li, X. Ren, J. Liu, X. Liang, Preparation of silane–WO_3 film through sol–gel method and characterization of photochromism, Thin Solid Films. 516 (2008) 5541–5544.

[13] W. Morales, M. Cason, O. Aina, N.R. Tacconi, K. Rajeshwar, Combustion synthesis and characterization of nanocrystalline WO_3, J. Am. Chem. Soc. 130 (2008) 6318–6319.

[14] A.M. Cruz, D.S. Martínez, E.L. Cuéllar, Synthesis and characterization of WO_3 nanoparticles prepared by the precipitation method: evalution of photocatalytic activity under vis–irradiation, Solid State Sci. 12 (2010) 88–94.

[15] X.C. Song, Y.F. Zheng, E. Yang, Y. Wang, Large–scale hydrothermal synthesis of WO_3 nanowires in the presence of K_2SO_4, Mater. Lett. 61 (2007) 3904–3908.

[16] C. Balázsi, L. Wang, E.O. Zayim, I.M. Szilágyi, K. Sedlacková, J. Pfeifer, A.L. Tóth, P.I. Gouma, Nanosize hexagonal tungsten oxide for gas sensing applications, J. Ceram. Soc. 28 (2008) 913–917.

[17] Z. Gu, H. Li, T. Zhai, W. Yang, Y. Xia, Y. Ma, J. Yao, Large–scale synthesis of single–crystal hexagonal tungsten trioxide nanowires and electrochemical lithium intercalation into the nanocrystals, J. Solid State Chem. 180 (2007) 98–105.

[18] C.M. White, J.S. Jang, S.H. Lee, J. Pankow, A.C. Dillon, Photocatalytic activity and photoelectrochemical property of nano–WO_3 powders made by hot–wire chemical vapor deposition, Electrochem. Solid State Lett. 13 (2010) B120–B122.

[19] E. Zelazowska, E.R. Pasek, WO_3–based electrochromic system with hybrid organic–inorganic gel electrolytes, J. Non–Cryst. Solids. 354 (2008) 35–39.

[20] B. Munro, S. Krämer, P. Zapp, H. Krug, Characterization of electrochromic WO_3–layers prepared by sol–gel nanotechnology, J. Sol–Gel Sci. Technol. 13 (1998) 673–678.

[21] K.D. Lee, Deposition of WO_3 thin films by the sol–gel method, Thin Solid Films. 302 (1997) 84–88.

[22] N. Asim, S. Radiman, M.A. Yarmo, Synthesis of WO_3 in nanoscale with the usage of sucrose ester microemulsion and CTAB micelle solution, Mater. Lett. 61 (2007) 2652–2657.

[23] A. Phuruangrat, D.J. Ham, S.J. Hong, S. Thongtem, J.S. Lee, Synthesis of hexagonal WO_3 nanowires by microwave–assisted hydrothermal method and their electrocatalytic activities for hydrogen evolution reaction, J. Mater. Chem. 20 (2010) 1683–1690.

[24] D.B. Hernández–Uresti, D. Sánchez–Martínez, A.M. Cruz, S. Sepúveda–Guzmán, L.M. Torres–Martínez, Photocatalytic degradation of organic compounds by $PbMoO_4$ synthesized by a microwave–assisted solvothermal method. Ceram. Int. 42 (2014) 3096–3103.

[25] R.D. Kumar, S. Karuppuchamy, Microwave–assisted synthesis of copper tungstate nanopowder for supercapacitor applications, Ceram. Int. 40 (2014) 12397–12402.

[26] H. Matsui, Y. Saitou, S. Karuppuchamy, M.A. Hassan, M. Yoshihara, Photo–electronic behavior of Cu_2O–and/or CeO_2–loaded TiO_2/carbon cluster nanocomposite materials, J. Alloys Compd. 538 (2012) 177–182.

[27] H. Matsui, S. Nagano, S. Karuppuchamy, M. Yoshihara, Synthesis and characterization of TiO_2/MoO_3/carbon clusters composite material, Curr. Appl. Phys. 9 (2009) 561–566.

[28] H. Matsui, T. Okajima, S. Karuppuchamy, M. Yoshihara, The electronic behavior of V_2O_3/TiO_2/carbon clusters composite materials obtained by the calcination of a $V(acac)_3$/TiO $(acac)_2$/polyacrylic acid complex, J. Alloys Compd. 468 (2009) 27–32.

[29] S. Karuppuchamy, N. Suzuki, S. Ito, T. Endo, A novel one–step electrochemical method to obtain crystalline titanium dioxide films at low temperature, Curr. Appl. Phys. 9 (2009) 243–248.

[30] M. Kovendhan, D.P. Joseph, E.S. Kumar, A. Sendikumar, P. Manimuthu, S. Sambasivam, C.

Venkateswaran, R. Mohan, Structural transition and blue emission in textured and highly transparent spray deposited Li doped WO_3 thin films, Appl. Surf. Sci. 257 (2011) 8127–8133.

[31] S. Dabbous, A. Arfaoui, K. Boubaker, A. Colantoni, L. Longo, M. Amlouk, Comparative study of indium and zinc doped WO_3 self–organized porous crystals in terms of nano–structural and opto–thermal patterns, Mater. Sci. Semicond. Process. 18 (2014) 171–177.

[32] A. Rougier, F. Portemer, A. Quédé, A.E. Marssi, Characterization of pulsed laser deposited WO_3 thin films for electrochromic devices, Appl. Surf. Sci. 153 (1999) 1–9.

[33] H. Habazaki, Y. Hayashi, H. Konno, Characterization of electrodeposited WO_3 films and its application to electrochemical wastewater treatment, Electrochim Acta. 47 (2002) 4181–4188.

[34] D. Ye, D. Li, W. Zhang, M. Sun, Y. Hu, Y. Zhang, X. Fu, A new photocatalyst $CdWO_4$ prepared with a hydrothermal method, J. Phys. Chem. C. 112 (2008) 17351–17356.

[35] C. Hu, C.Y. Jimmy, Z. Hao, P.K. Wong, Photocatalytic degradation of triazine–containing azo dyes in aqueous TiO_2 suspensions, Appl. Catal. B: Environ. 42 (2003) 47–55.

[36] X. Li, G. Zhang, F. Cheng, B. Guo, J. Chen, Synthesis, characterization, and gas–sensor application of WO_3 nanocuboids, J. Electrochem. Soc. 153 (2006) H133–H137.

[37] H.B. Huang, Y. Wang, W.B. Jiao, F.Y. Cai, M. Shen, S.G. Zhou, H.L. Cao, J. Lü, R. Cao, Lotus–leaf–derived activated–carbon–supported nano–CdS as energy–efficient photocatalysts under visible irradiation, ACS Sustainable Chem. Eng. 6 (2018) 7871−7879.

[38] H.B. Huang, Y. Wang, F.Y. Cai, W.B. Jiao, N. Zhang, C. Liu, H.L. Cao, J. Lü, Photodegradation of rhodamine B over biomass–derived activated carbon supported CdS nanomaterials under visible irradiation, Front. Chem. 5 (2017) 00123.

[39] F. Jing, R. Liang, J. H. Xiong, R. Chen, S. Y. Zhang, Y.H. Li, L. Wu, MIL–68(Fe) as an

efficient visible–light–driven photocatalyst for the treatment of a simulated waste–water contain Cr(VI) and malachite green. Appl. Catal., B 206 (2017) 9−15.

[40] H.B. Huang, N. Zhang, K. Yu, Y.Q. Zhang, H.L. Cao, J. Lü, R. Cao, One–step carbothermal synthesis of robust CdS@BPC photocatalysts in the presence of biomass porous carbons, ACS Sustainable Chem. Eng. 7 (2019a) 16835−16842.

[41] H.L. Cao, F.Y. Cai, K. Yu, Y.Q. Zhang, J. Lü, R. Cao, Photocatalytic degradation of tetracycline antibiotics over CdS/nitrogen–doped–carbon composites derived from in situ carbonization of metal–organic frameworks, ACS Sustainable Chem. Eng. 7 (2019) 10847–10854.

[42] H.B. Huang, K. Yu, J.T. Wang, J.R. Zhou, H.F. Li, J. Lü, R. Cao, Controlled growth of ZnS/ZnO heterojunctions on porous biomass carbons via one–step carbothermal reduction enables visible–light–driven photocatalytic H_2 production, Inorg. Chem. Front. 6 (2019b) 2035–2042.

[43] Y.X. Yan, H. Yang, Z. Yi, T. Xian, R.S. Li, X.X. Wang, Construction of Ag_2S@$CaTiO_3$ heterostructure photocatalysts for enhanced photocatalytic degradation of dyes, Desalin. Water Treat. 170 (2019) 349–360.

[44] Y.X. Yan, H. Yang, Z. Yi, X.X. Wang, R.S. Li, T. Xian, Evolution of Bi nanowires from BiOBr nanoplates through a $NaBH_4$ reduction method with enhanced photodegradation performance, Environ. Eng. Sci. 37 (2020) 64–77.

Conflict of Interest Statement

The authors declare that the research was conducted in the absence of any commercial or financial relationships that could be construed as a potential conflict of interest.